PHYSICAL REVIEW A VOLUME 16, NUMBER 4 OCTOBER 1977

Double photoionization of neon and argon*

Steven L. Carter and Hugh P. Kelly
Department of Physics, University of Virginia, Charlottesville, Virginia 22901
(Received 8 April 1977)

Many-body perturbation theory is applied to calculate double-electron photoionization for neon and argon. Cross sections for the outer-shell np^2 and $nsnp$ pair excitations are included in both the dipole-length and dipole-velocity formulations. Results are in generally good agreement with recent experimental data.

I. INTRODUCTION

Current interest in the phenomena involving multiple electron ionization is evidenced by recent experimental work in the rare gases,[1-5] where it is known that these processes can contribute a substantial percentage of the total ionization cross section. For neon and argon, independent studies in multiple ionization from both photon and electron impact have shown relatively good agreement and provide the impetus for careful theoretical analysis by means of calculations which include correlation effects. Theoretical calculations which include these effects are desirable for an accurate description of multiple photoionization processes, and important work has been done for helium,[6] beryllium,[7] and neon.[8,9]

In this paper we present the results of a calculation of the total double-electron photoionization cross sections $\sigma^{2+}(\omega)$ for both neon and argon in the energy range extending to 200 eV above threshold. We have applied the many-body perturbation theory (MBPT) of Brueckner[10] and Goldstone[11] using the techniques developed for application of this theory to atoms.[12] As in previous work[13] we have extended the MBPT prescription with a supplemental development in Rayleigh-Schrödinger perturbation theory (RSPT) using LS-coupled wave functions for the basis set. The numerical techniques used in applying MBPT to atoms are equally applicable in applying RSPT to many-electron systems. Use of RSPT in this work allows one to distinguish LS core-structure effects and to make use of experimentally determined two-electron removal energies. New insight into the double photoionization process is provided by detailed analysis of *multiple* partial-wave excitations from both np^2 and $nsnp$ outer-shell electron pairs, where it is found, in particular, that the $nsnp$ transitions contribute a substantial fraction of the total $\sigma^{2+}(\omega)$.

Details of the theory are presented in Sec. II. Section III contains a discussion of special computational techniques and numerical results for the total $\sigma^{2+}(\omega)$. A summary follows in Sec. IV.

II. THEORY

To calculate $\sigma^{2+}(\omega)$, a perturbation expansion is developed for the imaginary part of the frequency-dependent dipole polarizability[12] $\alpha(\omega)$ for use in the relation[14]

$$\sigma^{2+}(\omega) = (4\pi/c)\omega \,\mathrm{Im}\alpha(\omega), \tag{1}$$

where ω is the photon energy and c is the speed of light. Atomic units are employed throughout except where noted otherwise.

Neglecting the spin-orbit interaction and other relativistic effects, the expansion for $\mathrm{Im}\alpha(\omega)$ is applied to an atom with atomic Hamiltonian

$$H = H_0 + H_c, \tag{2}$$

where

$$H_0 = \sum_{i=1}^{N} -\frac{\nabla_i^2}{2} - \frac{Z}{r_i} + V(r_i) \tag{3}$$

and

$$H_c = \sum_{i<j=1}^{N} v_{ij} - \sum_{i=1}^{N} V(r_i). \tag{4}$$

The term v_{ij} represents the Coulomb interaction between electron pairs, and the single-particle potential $V(r_i)$ is chosen to account for the average interaction of the ith electron with the other $N-1$ electrons.

In the dipole approximation, a perturbing electric field $F\hat{z}\cos wt$ adds to H_c a term of the form

$$V_{ex}(r,t) = F\cos wt \sum_{i=1}^{N} z_i, \tag{5}$$

which leads to an expression for $\mathrm{Im}\alpha(\omega)$ in terms of the dipole matrix element. For double-electron photoionization, the dipole-length matrix elements are given by

$$Z(pq \to k'k) = \langle \Psi_f | \sum_{i=1}^{N} z_i | \Psi_0 \rangle, \tag{6}$$

where Ψ_0 and Ψ_f are many-particle ground and continuum states, respectively, with Ψ_f representing the excitation of an electron pair from ground-state

orbitals p and q to excited-state orbitals k' and k. The dipole velocity-form matrix element is obtained by replacing the matrix element in Eq. (6) by

$$(E_0 - E_f)^{-1}\langle\Psi_f|\sum_{i=1}^{N}\frac{d}{dz_i}|\Psi_0\rangle, \tag{7}$$

where E_0 and E_f are energy eigenvalues corresponding to Ψ_0 and Ψ_f.

In lowest order, Ψ_0 becomes the unperturbed state Φ_0 given by

$$H_0\Phi_0 = E_0^{(0)}\Phi_0, \tag{8}$$

where Φ_0 is represented in the Russell-Saunders LSM_LM_S coupling scheme as a linear combination of determinants, each containing N different single-particle states ϕ_n which are solutions of

$$[-\tfrac{1}{2}\nabla^2 - Z/r + V(r)]\phi_n = \epsilon_n\phi_n. \tag{9}$$

In this representation, for example, the lowest-order energy $E_0^{(0)}$ of Eq. (8) is given by

$$E_0^{(0)} = \sum_{i=1}^{N}\epsilon_i. \tag{10}$$

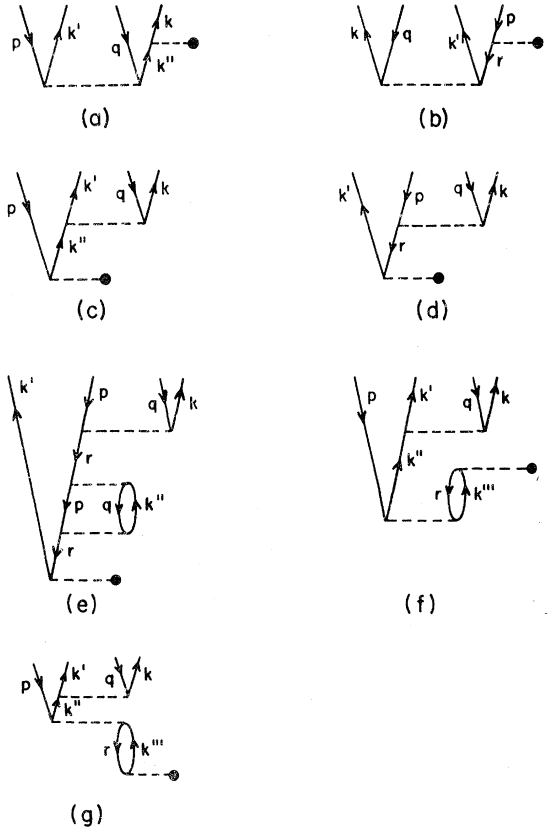

FIG. 1. Diagrams contributing to the matrix element $Z(pq \to k'k)$. Full circles indicate matrix element of z; broken lines represent Coulomb interactions. Exchange diagrams are also included.

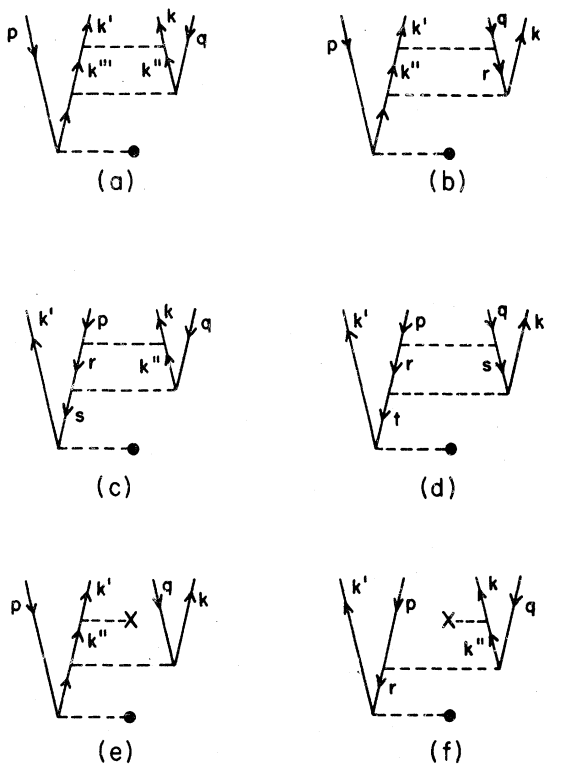

FIG. 2. Second-order diagrams associated with electron screening effects. The cross indicates interaction with the potential (included in H_c). Exchange diagrams are also included.

The excited-state single-particle continuum orbitals are normalized in the k scale[15] according to

$$P_k(r) = rR_k(r)$$
$$= \cos[kr + (q/k)\ln(2kr) - \tfrac{1}{2}\pi(l-1) + \delta_l], \tag{11}$$

where $V(r) \to q/r$ as $r \to \infty$. With this choice of normalization Eq. (1) becomes

$$\sigma^{2+}(\omega) = \frac{16\omega}{c}\int_0^{k_{\max}} dk\ \frac{|Z(pq \to k'k)|^2}{k'}, \tag{12}$$

where

$$k' = [2(\epsilon_p + \epsilon_q - \tfrac{1}{2}k^2 + \omega)]^{1/2},$$
$$k_{\max} = [2(\epsilon_p + \epsilon_q + \omega)]^{1/2}.$$

Individual terms in the perturbation expansion for $Z(pq \to k'k)$ involve single-particle states and may be represented by open diagrams of the form shown in Figs. 1 and 2. The lowest-order double photoionization diagrams contain one dipole interaction and one interaction with the electron-correlation perturbation H_c of Eq. (4) as shown in Figs. 1(a)-1(d). The time ordering of the interactions proceeds graphically from bottom to top, with diagrams 1(a) and 1(b) representing ground-state cor-

relations (GSC) and diagrams 1(c) and 1(d) representing final-state correlations (FSC). Particular higher-order diagrams of interest are shown in Figs. 1(e)-1(g).

Exchange diagrams are always understood to be included. For example, the exchange diagram of Fig. 1(a) corresponds to an interchange (at the Coulomb interaction vertices) of either the p and q hole lines or the k' and k'' particle lines. A simultaneous interchange of both pairs does not form a diagram distinct from Fig. 1(a).

Certain exclusion-principle-violating (EPV) diagrams may arise from interactions with the potential (included in H_c) and from the factorization of unlinked diagrams[12] in the expansion for $Z(pq \rightarrow k'k)$. Such diagrams can represent important physical effects and usually appear in the form shown in Fig. 1(d) with $r=p$. The Coulomb interaction portion of this diagram, for example, in the case where $r=p$, and q and k have the same angular momentum quantum number, is closely related to the monopole transition (electron shakeoff)[5] matrix element.

The general form of the energy denominators occurring in GSC diagrams is

$$D=\sum_{i=1}^{N'}(\epsilon_{p_i}-\epsilon_{k_i}) \tag{13a}$$

and for FSC diagrams,

$$D=\sum_{i=1}^{N'}(\epsilon_{p_i}-\epsilon_{k_i})+\omega\,, \tag{13b}$$

where ϵ_{p_i} and ϵ_{k_i} are single-particle energies for a hole-particle energies for a hole-particle pair, and N' is the number of pairs excited. In Eq. (13b) the cases in which the denominator may vanish are treated according to

$$\lim_{n\rightarrow 0}(D+i\eta)^{-1}=\mathrm{P}D^{-1}-i\pi\delta(D)\,, \tag{14}$$

where P represents principal-value integration.

Certain classes of diagrams may be summed geometrically to produce shifts[12] in the single-particle energies corresponding to energy correlations. They are included semiempirically by replacing the sum over single-particle energies ϵ_{p_i} of Eq. (13) with minus the experimental removal energy. Shifts should also be applied to the excited-state single-particle energies. However, in most cases these shifts are small, and in this work all excited-orbital energies were taken to be Hartree-Fock (HF) frozen-core calculated values.

A special type of denominator shift can be illustrated in Fig. 1(d). The physical excitation processes for this diagram might be described as follows. The inner-shell electron r is the primary photoelectron excited to the continuum orbital k' through the dipole interaction. An outer-shell p electron then fills the unoccupied r orbital with a simultaneous ejection of electron q to the continuum orbital k. The unperturbed energy denominator for this "virtual-Auger"[8,9] process of diagram 1(d) is given by

$$D=\epsilon_r-\epsilon_{k'}+(-\epsilon_p-\epsilon_q+\epsilon_{k'}+\epsilon_k), \tag{15}$$

where the term in parentheses corresponds to the photon energy ω. Equation (15) is the lowest-order approximation to the energy difference between the final and intermediate states and can vanish for the special case when

$$\epsilon_k=-\epsilon_r+\epsilon_p+\epsilon_q. \tag{16}$$

Since energy is then conserved between the intermediate and final states, diagram 1(d) also accounts for the possibility of certain Auger transitions.

The singularity in Eq. (15) can be removed by including higher-order diagrams such as shown in Fig. 1(e). Diagrams 1(d) and 1(e) together form the first two terms of a geometric series with ratio

$$R=[-i\tfrac{1}{2}\Gamma(\omega)+\Delta(\omega)]/D, \tag{17}$$

where

$$\tfrac{1}{2}\Gamma(\omega)=(2/k)\left|\langle\Phi_r^{k'}|v|\Phi_{pq}^{k'k}\rangle\right|^2 \tag{18}$$

and

$$\Delta(\omega)=\frac{2}{\pi}\mathrm{P}\int dk''\,\frac{\left|\langle\Phi_r^{k'}|v|\Phi_{pq}^{k'k''}\rangle\right|^2}{\epsilon_p+\epsilon_q-\epsilon_{k'}-\epsilon_{k''}+\omega}\,. \tag{19}$$

In Eqs. (18) and (19), $\Phi_r^{k'}$ is the HF wave function for the intermediate state in which the inner-shell electron r has been excited to the continuum orbital k'. Similarly, $\Phi_{pq}^{k'k''}$ represents the HF wave function for the state in which electrons p and q have been excited to continuum orbitals k' and k''. The term Δ is interpreted as a contribution to the correlation energy[12] of the $\Phi_r^{k'}$ state. The term $\frac{1}{2}\Gamma$ is a lowest-order width associated with the $\Phi_r^{k'}$ state and determines the Auger rate for that state. Both of the terms Δ and $\frac{1}{2}\Gamma$ arise from the integration over k'' in diagram 1(e) in which the energy denominator is treated according to Eq. (14). In final form, with $D'=D+\Delta(\omega)$, diagram 1(d) may be expressed as

$$\frac{D'-i(\frac{1}{2}\Gamma)}{D'^2+(\frac{1}{2}\Gamma)^2}\langle\Phi_{pq}^{k'k}|v|\Phi_r^{k'}\rangle\langle\Phi_r^{k'}|z|\Phi_0\rangle\,, \tag{20}$$

where the ω dependence of $\frac{1}{2}\Gamma$ and D' is understood. Note that both real and imaginary pieces contribute in the expansion for $Z(pq\rightarrow k'k)$.

TABLE I. Argon dipole transitions.

State [a]		Contribution [b] (%) ω (eV) = 89.8	100.7	239.5
$3s^2 3p^6\ ^1S \rightarrow 3s^2 3p^4(^3P, ^1D, ^1S)$	$kskp(L')^1P$	6.7	5.6	2.4
	$kpkd$	64.1	59.8	46.1
	$kskf$	1.8	2.4	1.7
	$kdkf$	6.7	9.4	24.2
$3s^2 3p^6\ ^1S \rightarrow 3s3p^5(^3P, ^1P)$	$k'pkp(L')^1P$	9.8	9.7	7.9
	$k'dkd$	1.4	1.7	7.2
	$kskd$	9.5	11.4	10.5

[a] Notation (L') indicates that all allowed terms of the $k'k$ electron pair are to be included which are consistent with the intermediate- and final-state coupling.
[b] Geometric mean of length and velocity curves (see Ref. 23).

III. CALCULATIONS AND RESULTS

A. Methods of calculation

For both neon and argon, the transition matrix elements $Z(p,q \rightarrow k'k)$ of Eq. (6) were calculated for two principal cross sections. The first corresponds to photoejection of the outer-shell np^2 electron pair leaving the np^4 core configuration coupled to ^3P, ^1D, or ^1S. The second corresponds to excitation of an $nsnp$ electron pair leaving the $nsnp^5$ core coupled to either ^3P or ^1P. The allowed dipole-transition final-state configurations and terms are listed in Tables I and II for argon and neon, respectively. Also listed are the calculated relative contributions of each configuration to the total cross section. The selected angular-momentum quantum numbers of the excited $k'lkl$ electron pairs were the ones expected to give the largest contributions to $\sigma^{2+}(\omega)$. In a more complete treatment, additional combinations from higher l values and from other inner-shell excitations should also be included.

Sets of excited bound and continuum orbitals were calculated using the Hartree-Fock V^{N-1} potential.[12,16] Where appropriate, a projection-operator technique[17] was used to ensure orthogonality of excited- and ground-state orbitals. For each l value, eight bound excited states were explicitly included, with the contribution from the remainder approximated by the n^{-3} rule.[12] For sums over states, the continuum was approximated by 30 orbitals ranging from $k = 0.0625$ to 24.0.

In the MBPT approach, the lowest-order correlated matrix element $Z(pq \rightarrow k'k)$ is constructed from the sum of the first four diagrams of Fig. 1 with one calculation for each $pq \rightarrow k'k$ excitation in which the individual $ls\, m_l m_s$ electron quantum numbers are consistent with those of the single ground-state determinant. Using the RSPT method, $Z(pq \rightarrow k'k)$ is constructed for each of the possible transitions listed in Tables I and II using LS-coupled wave functions for the basis set. In both methods the final matrix element $Z(pq \rightarrow k'k)$ is numerically represented as a square matrix of ten preselected continuum k values ranging from $k = 0.0625$ to 5.0. The finer k mesh required for the integration in Eq. (12) is developed via a four-point Lagrange inter-

TABLE II. Neon dipole transitions.

State [a]		Contribution [b] (%) ω (eV) = 130.6	160.5	278.0
$2s^2 2p^6\ ^1S \rightarrow 2s^2 2p^4(^3P, ^1D, ^1S)$	$kskp(L')^1P$	4.3	3.4	3.1
	$kpkd$	74.0	69.9	52.4
	$kskf$	1.9	1.9	1.8
	$kdkf$	2.2	3.1	5.8
$2s^2 2p^6\ ^1S \rightarrow 2s2p^5(^3P, ^1P)$	$k'sks(L')^1P$	0.5	0.5	0.4
	$k'pkp$	13.9	15.1	21.6
	$kskd$	2.9	5.4	10.5
	$k'dkd$	0.2	0.4	2.7
	$kpkf$	0.1	0.3	1.2
	$k'fkf$	0.01	0.04	0.5

[a] Notation (L') indicates that all allowed terms of the $k'k$ electron pair are to be included which are consistent with the intermediate- and final-state coupling.
[b] Geometric mean of length and velocity curves (see Ref. 23).

polation procedure which can be appropriately adjusted for each photon energy ω.

The individual diagrams of Fig. 1 are normally evaluated in the usual manner by a sum over intermediate bound states and integral over the continuum. Diagram 1(a), however, is difficult to evaluate by this technique because of the radial integrations in the k'' to k dipole matrix elements when both k'' and k represent continuum spin orbitals. An alternative method involves application of the differential-equation or effective-operator approach which has been used successfully by other authors.[8,9,18,19] In radial form (quantities with subscript R refer to radial parts only) diagram 1(a) becomes

$$D_R = \sum_{k''} \frac{\langle k|r|k''\rangle_R \langle k'k''|v|pq\rangle_R}{\epsilon_p + \epsilon_q - \epsilon_{k'} - \epsilon_{k''}}, \tag{21}$$

where v represents the radial part of the Coulomb interaction and where the sum over k'' is limited to excited single-particle states. If one defines $|\Psi_{k'}\rangle_R$ such that

$$|\Psi_{k'}\rangle_R = \sum_{k''} \frac{|k''\rangle_R \langle k'k''|v|pq\rangle_R}{\epsilon_p + \epsilon_q - \epsilon_{k'} - \epsilon_{k''}}, \tag{22}$$

then D_R is evaluated according to

$$D_R = \langle k|r|\Psi_{k'}\rangle_R. \tag{23}$$

Letting $E = \epsilon_p + \epsilon_q - \epsilon_{k'}$, Eq. (22) takes on the form

$$(E - H_0)|\Psi_{k'}\rangle_R = \sum_{k''} |k''\rangle_R \langle k'k''|v|pq\rangle_R. \tag{24}$$

Applying closure, one obtains the equation

$$(E - H_0)|\Psi_{k'}\rangle_R = F(r), \tag{25}$$

where

$$F(r) = \left(\frac{1}{r^{\kappa+1}} \int_0^r dr' r'^{\kappa} P_{k'}(r') P_p(r') + r^{\kappa} \int_r^{\infty} dr' P_{k'}(r') P_p(r')\right) P_q(r) - \sum_{n''_{\rm occ}} |n''\rangle_R \langle k'n''|v|pq\rangle_R. \tag{26}$$

In Eqs. (24) and (25), H_0 is defined as in Eq. (9). The term $P_i(r)$ is the radial part of the ith spin orbital contained in the Coulomb matrix element of Eq. (24), and κ is the appropriate kappa value. The sum over $n''_{\rm occ}$ refers to any bound, occupied orbitals which must be projected out of Eq. (24) to effect closure. For large r the function $F(r)$ approaches zero, and since $E < 0$, the solution $|\Psi_{k'}\rangle_R$ has the nature of a bound function. Substitution of $|\Psi_{k'}\rangle_R$ into Eq. (23) completes the evaluation of the diagram.

B. Argon

The total $\sigma^{2+}(\omega)$ for argon is shown in Fig. 3 for both dipole-length and dipole-velocity matrix elements (a preliminary account of these results was presented previously[20]). These curves are the direct sum of 30 individual cross sections represented according to the LS-coupled terms and configurations of Table I. The net contribution of each partial-wave configuration (as a percentage) is also

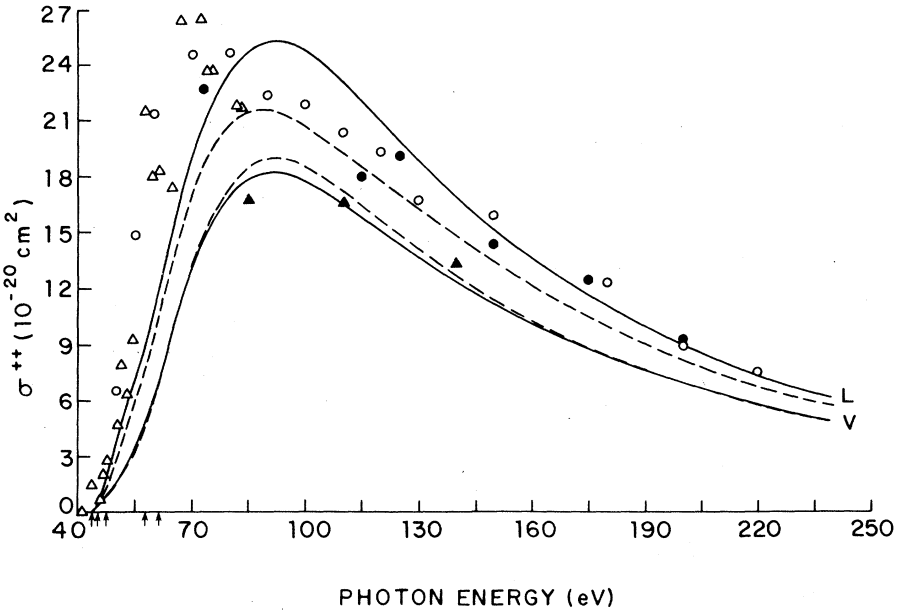

FIG. 3. Total $\sigma^{2+}(\omega)$ for neutral argon. Full curves are lowest-order results for dipole-length (L) and dipole-velocity (V) matrix elements. Broken curves include second-order correlations. Experimental data points are from Schmidt *et al.* (Ref. 1), full circles; Wight and Van der Wiel (Ref. 2), open circles; Samson and Haddad (Ref. 3), open triangles; Carlson (Ref. 5); full triangles. Arrows mark, respectively, experimental (Ref. 24) excitation thresholds for the $3s^2 3p^4(^3P, ^1D, ^1S)$ and $3s3p^5(^3P, ^1P)$ core configurations.

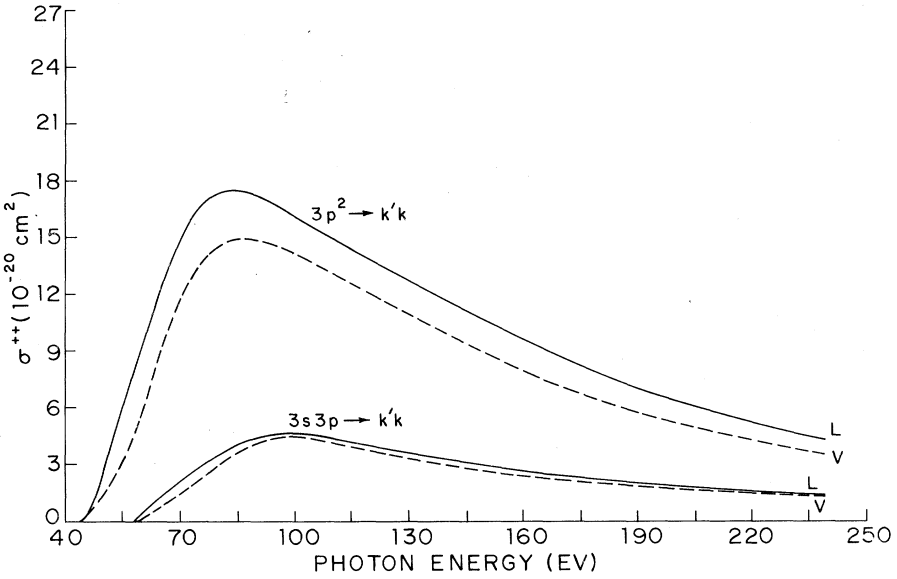

FIG. 4. Cross sections for the total $3p^2 \rightarrow k'k$ and $3s3p \rightarrow k'k$ excitations in neutral argon. Results are plotted for both dipole-length (solid curves) and dipole-velocity (broken curves) matrix elements.

listed in Table I for three values of incident photon energy. The first, at 89.8 eV, corresponds to the maximum of the total $\sigma^{2+}(\omega)$. The second, at 100.7 eV, corresponds to the maximum in the total contribution from $3s3p \rightarrow k'k$ excitations. The final point at 239.5 eV is the highest ω value calculated. The trend toward a higher relative contribution from the $3s3p$ transitions becomes evident as the photon energy increases. Figure 4 illustrates this by separately showing the component $3p^2$ and $3s3p$ contributions to Fig. 3. Note that for $\omega = 239.5$ eV, the $3s3p$ transitions account for more than 25% of the total $\sigma^{2+}(\omega)$.

The solid curves in Fig. 3 represent lowest-order results and are calculated from the first four diagrams of Fig. 1 for each partial-wave combination. Selected higher-order terms such as shown in Figs. 1(f) and 1(g) were also calculated because the lower portions (dipole and Coulomb interactions) of these two diagrams are know from previous work in argon[21] to provide important correlations in the $p \rightarrow k''$ dipole matrix elements. As indicated by the broken curves in Fig. 3, addition of these diagrams yielded substantial second-order corrections, particularly in the region near maximum. The relatively small change in the velocity-form curve may indicate that this is the more accurate of the two forms in low order although there

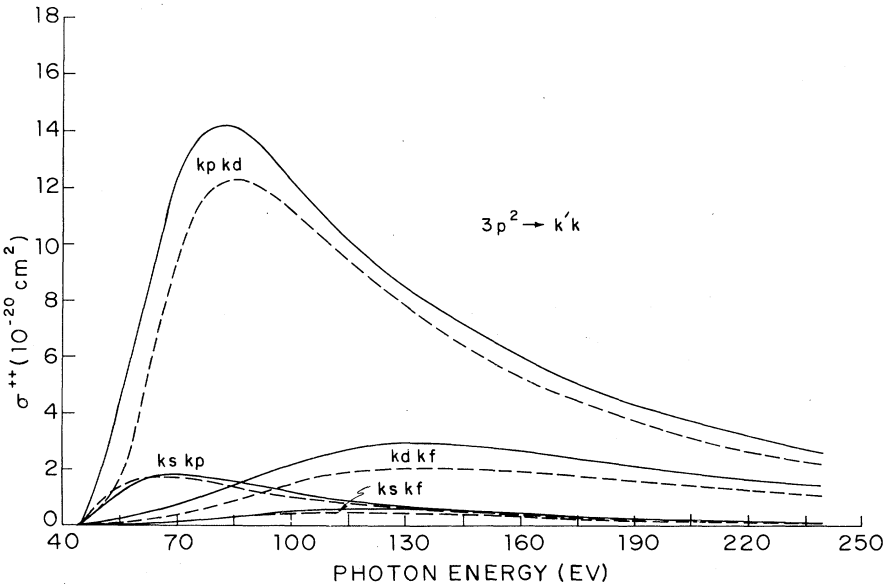

FIG. 5. Partial-wave cross sections for the four $3p^2 \rightarrow k'k$ channels of Table I. Results are plotted for both dipole-length (solid curves) and dipole-velocity (broken curves) matrix elements.

is the possibility that further addition of higher-order FSC diagrams such as shown in Figs. 2(a)-2(f) might produce significant correlations.

Experimental data points in Fig. 3 were normalized with the total argon photoionization cross section of West and Marr,[22] using values for the ratio $R=\sigma^{2+}/\sigma^{+}$ as determined in the experiments,[1-3,5] and assuming that σ^{3+} is approximately zero. The data from Samson and Haddad[3] have been included only for the energy range below the triple photoionization threshold at 84.3 eV, since above this value their results presumably show a large amount of σ^{3+}.

The correlated length-form curve of Fig. 3 shows the best overall agreement with experiment; however, the interpretation that the length-form curve is more accurate is probably incorrect. It is more likely that, for the partial-wave configurations included, the true cross section is bracketed by the correlated curves of Fig. 3 and is thus below experiment. It is expected that inclusion of other excitation channels (e.g., $3p^2 \rightarrow kpkg$, $kfkg$, etc.; $3s3p \rightarrow kpkf$, $kdkg$, etc.; and $3s^2 \rightarrow k'k$) might contribute the additional 10-15% increase necessary for closer agreement. Figure 5, for example, shows length and velocity curves for the four $3p^2 \rightarrow k'k$ channels listed in Table I. Based on the general form and amplitude of these curves, it is not unreasonable to expect that contributions from higher l-value partial waves and from other inner-shell excitations would improve agreement with experiment. Addition of the second-order diagrams of Fig. 2 is also expected to shift the maximum position and initial slope of the calculated curves to more closely match the experimental result. Further discussion of these diagrams is presented in the next section.

C. Neon

The total $\sigma^{2+}(\omega)$ for neon is shown in Fig. 6 for both dipole-length and dipole-velocity matrix elements. These curves are the direct sum of 40 lowest-order cross sections represented according to the terms and configurations of Table II. As in argon, the net percentage contribution of each partial-wave excitation is listed for three representative photon energies. Experimental data points in Fig. 6 were again normalized according to the total neon photoionization cross section of West and Marr[22] using values for the ratio $R=\sigma^{2+}/\sigma^{+}$ as determined in the experiments.[1-5]

The neon results are qualitatively similar to those for argon with the exception that the discrepancy with experiment of the neon $\sigma^{2+}(\omega)$ maximum position and initial slope is more pronounced than in argon. For higher photon energies, however, the agreement is generally better. The displacement of the calculated maximum position to the right in Fig. 6, and to a lesser degree in Fig. 3, may be due to screening effects. Since all continuum wave functions are calculated in the HF V^{N-1} potential, the one-electron orbitals are not particularly appropriate for use in evaluating matrix elements corresponding to double excitation processes. This is reflected by the asymptotic form shown in Eq. (11), where $V(r) \rightarrow 1/r$ as $r \rightarrow \infty$. More correctly then, the outgoing electron wave functions could be calculated in a V^{N-2} potential so that asymptotically, at least, the orbitals would more appropriately account for the net plus two charge of the residual ion. The picture is further complicated by the energy spectrum of the excited pair which shows that, in general, the available kinetic energy is unequally distributed. The faster electron may therefore be screened to some extent by the slower one, so one might argue that the faster electron "feels" a residual charge of approximately +1 while the slower electron sees a residual charge of approximately +2.

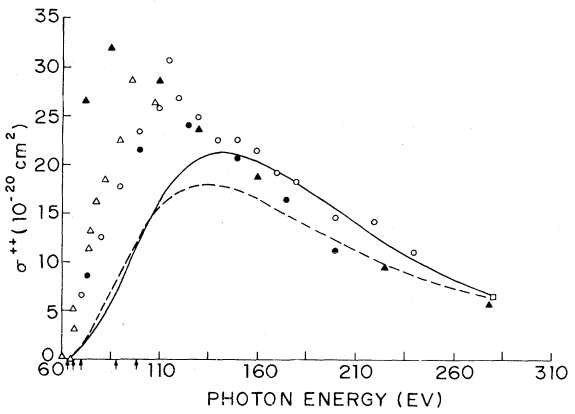

FIG. 6. Total $\sigma^{2+}(\omega)$ for neutral neon. Lowest-order results are shown for both dipole-length (solid curve) and dipole-velocity (broken curve) matrix elements. Experimental data points are from Schmidt *et al.* (Ref. 1), full circles; Wight and Van der Wiel (Ref. 2), open circles; Samson and Haddad (Ref. 3), open triangles; Carlson (Ref. 5), full triangles; Lightner *et al.* (Ref. 4), open square. Arrows mark, respectively, experimental (Ref. 24), excitation thresholds for the $2s^22p^4(^3P, ^1D, ^1S)$ and $2s2p^5(^3P, ^1P)$ core configurations.

Provided that enough terms in the perturbation expansion are included, the actual choice of potential should not affect final results. In lowest order, however, results can be quite different. It can be shown, for example, that the RSPT angular factors for the first four diagrams of Fig. 1 are identical for both the V^{N-1} and V^{N-2} potentials when used in conjunction with the projection-operator technique.[17] Since the radial wave functions of the ex-

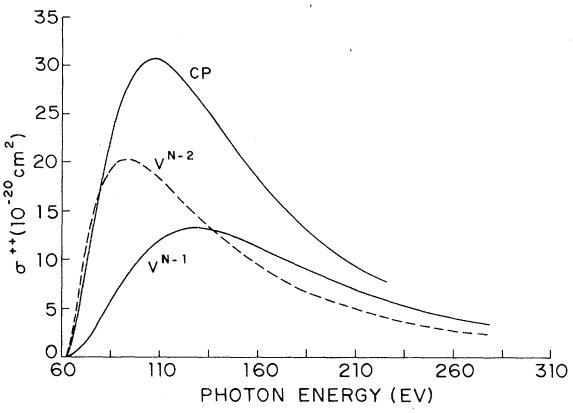

FIG. 7. Velocity-form cross sections for the neon $2p^2 \rightarrow kpkd$ excitation. Curve labeled $V^{N-1}(V^{N-2})$ corresponds to orbitals calculated in the HF $V^{N-1}(V^{N-2})$ potential. Curve labeled CP is from the calculation by Chang and Poe (Ref. 9).

cited-state orbitals are quite different for the two cases, the lowest-order $\sigma^{2+}(\omega)$ calculations will almost certainly be different. Details of the potential should affect the second-order diagrams of Fig. 2 in which electron-correlation interactions depend sensitively on the form chosen for $V(r)$ in Eq. (4). These diagrams are of the type associated with electron screening effects and would probably need to be included to produce agreement in $\sigma^{2+}(\omega)$ calculations for both choices of potential.

The curves shown in Fig. 7 may help to illustrate these points. Shown in the figure are two lowest-order, velocity-form calculations for the neon $2p^2 \rightarrow kpkd$ dipole excitation. For the curve labeled V^{N-1}, all excited-state orbitals were calculated using the HF V^{N-1} potential. The curve labeled V^{N-2} corresponds to orbitals calculated in a HF V^{N-2} potential based on the average configuration energy. The shift in size and position of the maximum is immediately apparent. Near threshold the slope of the V^{N-2} curve agrees better with experiment but is, in fact, too steep. The V^{N-2} maximum position also occurs earlier than that shown by experiment. Presumably, the correct $\sigma^{2+}(\omega)$ curve for the $2p^2 \rightarrow kpkd$ excitation lies somewhere intermediate between these two cases and should follow in either calculation from inclusion of the diagrams in Fig. 2. Since the areas under the V^{N-1} and V^{N-2} curves are approximately the same, the lowest-order oscillator strength appears to be relatively independent of the choice of potential. The overall shape of the cross section, however, is sensitive to the detailed structure of the potential and therefore dependent upon higher-order terms in the perturbation expansion for which this structure may be important.

The curve labeled CP in Fig. 7 is the $2p^2 \rightarrow kpkd$, velocity-form result from a MBPT calculation by Chang and Poe.[9] The large discrepancy between their result and our V^{N-1} curve is somewhat surprising since both calculations are based on V^{N-1} excited-state orbitals. Because of differences in computational technique, a detailed, term-by-term comparison of the two results is difficult. One contributing factor to differences in the two curves could be the omission of contributions to certain diagrams in the Chang and Poe calculation. In diagram 1(a), for example, the electron labeled k'' is allowed to represent s, p, d, and f excited-state orbitals, while Change and Poe have included only the p and d intermediate states. We find in our work that contributions from both s and f excitations (including angular factors) are non-negligible in many cases and are, in fact, comparable to those from the p and d excitations. However, a calculation in which the s and f contributions were omitted from the RSPT expansion shows, at most, a 20% increase over the original result and therefore does not fully account for the discrepancy. As a further test, because of the algebraic complexity involved in determining angular factors in both the RSPT and MBPT formalisms, we carried out a calculation using the usual MBPT formalism. In total, the MBPT and RSPT angular factors were found to agree exactly in both phase and magnitude and the resulting $kpkd$ velocity-form curve was essentially identical to the RSPT result.

Although our calculated V^{N-1} curve for the $2p^2 \rightarrow kpkd$ excitation shows less favorable agreement with experiment, it nevertheless is based on inclusion of *all* first-order diagrams and has been verified in both the MBPT and RSPT formalisms. While the CP curve initially shows better agreement with experiment, inclusion of other partial-wave channels (as shown by Table II) will push their result considerably above experiment. Further study of screening effects and choice of potential will be necessary to resolve the lack of agreement between calculations and experiment.

As a final consideration, it is of some interest to examine the kinetic-energy distribution of the photoejected electrons. Referring to Eq. (12), the energy spectrum is obtained by differentiating $\sigma^{2+}(\omega)$ with respect to ϵ_k. Since $\epsilon_k = \frac{1}{2}k^2$, we have

$$\frac{d\sigma^{2+}(\omega)}{d\epsilon_k} = \frac{dk}{d\epsilon}\frac{d\sigma^{2+}(\omega)}{dk} = \frac{16\omega}{c}\frac{|Z(pq \rightarrow k'k)|^2}{k'k},$$

where the matrix elements $Z(pq \rightarrow k'k)$ are constructed as in Eqs. (6) or (7). Dipole-velocity energy distribution curves are shown in Fig. 8 for $\omega = 278$ eV. Results are plotted separately for the total $2p^2 \rightarrow k'k$ and $2s2p \rightarrow k'k$ excitations. The curves are made symmetric by adding the distributions

from each outgoing electron. Peaks in the two curves correspond to differences in excitation thresholds for the five possible core-configuration terms shown in Table II. The tendency toward unequal sharing of the total available kinetic energy is indicated by the deep minima of Fig. 8, while for photon energies near threshold the same curves become much flatter. This behavior is typical in the double photoionization process and is in qualitative agreement with the findings by Carlson[5] and by Chang and Poe.[9]

IV. CONCLUSIONS

In summary, we find that a low-order perturbation calculation is sufficient to reproduce the essential features of the double photoionization process, while providing insight into the excitation mechanisms involved through electron-correlation and partial-wave analyses. Appreciable contributions arise from a number of partial-wave channels, and it is found that both np^2 and $nsnp$ pair excitations must be included to obtain good results.

Calculations for neutral argon show reasonably good agreement with experimental data although less favorable agreement is seen in the case of neon. Discrepancies between theoretical and experimental results may be due in part to screening and possibly core-polarization effects which may not be adequately accounted for in a first-order calculation. For low-Z atoms in particular it is expected that inclusion of higher-order terms will be necessary to provide close agreement with experiment.

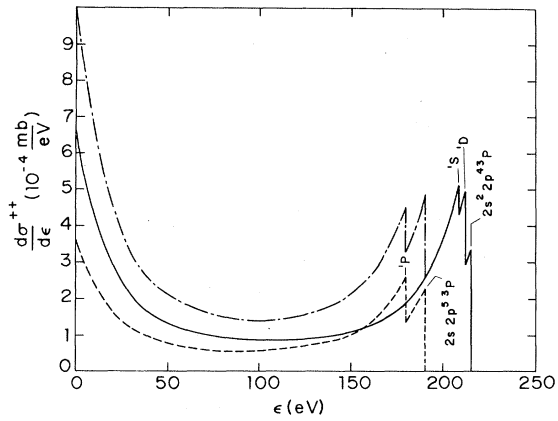

FIG. 8. Kinetic energy distributions for the neon $2p^2 \rightarrow k'k$ (solid curve) and $2s2p \rightarrow k'k$ (broken curve) excitations calculated at $\omega = 278$ eV. Chain curve is the sum of the two contributions.

We hope that this paper will stimulate further study of the multiple ionization process for both open- and closed-shell systems.

ACKNOWLEDGMENTS

We wish to thank Dr. V. Schmidt, Dr. T. A. Carlson, and Dr. T. N. Chang for generously supplying data and for helpful correspondence. We also thank Dr. C. F. Fischer for the Hartree-Fock code used in the calculation of ground-state orbitals. Suggestions from Dr. M. S. Pindzola and Dr. A. W. Fliflet are gratefully acknowledged.

*Work supported by the National Science Foundation.

[1]V. Schmidt, N. Sander, H. Kuntzemüller, P. Dhez, F. Wuilleumier, and E. Källne, Phys. Rev. A 13, 1748 (1976).
[2]G. R. Wight and M. J. Van der Wiel, J. Phys. B 9, 1319 (1976).
[3]J. A. R. Samson and G. N. Haddad, Phys. Rev. Lett. 33, 875 (1974).
[4]G. S. Lightner, R. J. Van Brunt, and W. D. Whitehead, Phys. Rev. A 4, 602 (1971).
[5]T. A. Carlson, Phys. Rev. 156, 142 (1967).
[6]F. W. Byron, Jr., and C. J. Joachain, Phys. Rev. 164, 1 (1967); R. L. Brown, Phys. Rev. A 1, 586 (1970); T. Åberg, Phys. Rev. A 2, 1726 (1970); M. Ya Amusia, E. G. Drukarev, V. G. Gorshkov, and M. P. Krazachkov, J. Phys. B 8, 1248 (1975).
[7]P.Winkler (unpublished).
[8]T. N. Chang, T. Ishihara, and R. T. Poe, Phys. Rev. Lett. 27, 838 (1971).
[9]T. N. Chang and R. T. Poe, Phys. Rev. A 12, 1432 (1975).
[10]K. A. Brueckner, Phys. Rev. 97, 1353 (1955); *The Many Body Problem* (Wiley, New York, 1959).
[11]J. Goldstone, Proc. R. Soc. A 239, 267 (1957).
[12]H. P. Kelly, Adv. Theor. Phys. 2, 75 (1968).
[13]S. L. Carter and H. P. Kelly, J. Phys. B 9, 1887 (1976).
[14]U. Fano and J. W. Cooper, Rev. Mod. Phys. 40, 441 (1968).
[15]H. A. Bethe and E. E. Salpeter, *Quantum Mechanics of One- and Two-Electron Atoms* (Springer-Verlag, Berlin, 1957).
[16]M. Ya. Amus'ya, N. A. Cherepkov, and L. V. Chernysheva, Zh. Eksp. Teor. Fiz. 60, 160 (1971) [Sov. Phys. JETP 33, 90 (1971)].
[17]L. M. Frantz, R. L. Mills, R. G. Newton, and A. M. Sessler, Phys. Rev. Lett. 1, 340 (1958); B. A. Lippmann, M. H. Mittleman, and K. M. Watson, Phys. Rev. 116, 920 (1959); R. T. Pu and E. S. Chang, *ibid.* 151, 31 (1966); H. J. Silverstone and M. L. Yin, J. Chem. Phys. 49, 2026 (1968); S. Huzinaga and C. Arnau, Phys. Rev. A 1, 1285 (1970).
[18]S. Garpman, I. Lindgren, J. Lindgren, and J. Morrison, Phys. Rev. A 11, 758 (1975).
[19]R. M. Sternheimer, Phys. Rev. 115, 1198 (1959).

[20]S. L. Carter and H. P. Kelly, J. Phys. B 9, L565 (1976).
[21]H. P. Kelly and R. L. Simons, Phys. Rev. Lett. 30, 529 (1973).
[22]J. B. West and G. V. Marr, Proc. R. Soc. A 349, 397 (1976).
[23]A. E. Hansen, Mol. Phys. 13, 425 (1967).
[24]C. E. Moore, *Atomic Energy Levels*, U.S. Natl. Bur. Stand. Circ. No. 467 (U. S. GPO, Washington, D.C., 1949).